ADVANCED FUNCTIONAL MATERIALS
www.afm-journal.de

Air Processing of Thick and Semitransparent Laminated Polymer:Non-Fullerene Acceptor Blends Introduces Asymmetric Current–Voltage Characteristics

Xabier Rodríguez-Martínez, Paula Hartnagel, Sergi Riera-Galindo, Gulzada Beket, Thomas Österberg, Feng Gao, Thomas Kirchartz, and Olle Inganäs*

Non-fullerene acceptors have recently revolutionized indoor organic photovoltaics (OPVs) with power conversion efficiencies exceeding 30% in laboratory scale. Nevertheless, transferring their superior performance to larger-scale prototyping, i.e., air-processing via roll-to-roll compatible techniques, still shows severe challenges. Herein, the industrial potential of the PM6:IO4Cl blend, which is one of the most successful indoor OPV photoactive layers (PALs), is thoroughly investigated. The corresponding thick and semitransparent laminated devices are fabricated entirely in air, by blade and slot-die coating. Their current–voltage (*J–V*) characteristics show anomalous features depending on the illumination side, with the cathode side generally outperforming the anode counterpart. Electrical and optical modeling reveal that a plausible cause of such a phenomenon is a dead layer that forms at the PAL/anode contact interface that does not contribute to the photocurrent. Said layer becomes undetectable when the PALs are made thin enough (<35 nm each) leading to symmetric *J–V* curves and improved light utilization efficiency. By screening the photovoltaic performance of multiple donor:acceptor blends, certain all-polymer and polymer:fullerene PALs are identified as adequately symmetric candidates for thick device up-scaling. Finally, ternary blends based on PM6:IO4Cl:fullerene may constitute a viable route to mitigate the electrical asymmetry detected on conventional binary blends.

1. Introduction

Indoor organic photovoltaics (OPVs) is emerging as off-grid power supply to replace or complement disposable batteries in a plethora of internet-of-things (IoT) devices.[1,2] Indoor OPVs are attractive for their semitransparency, favorable light in-coupling, and high power-per-weight ratio (W g^{-1}),[3,4] which allow integration of OPV modules in small-scale autonomous devices (e.g., in electronic shelf labels and audio headsets). Features, such as solution processability and flexibility are inherent to OPVs, hence enabling their industrialization in roll-to-roll (R2R) setups with sustainable life cycles.[5] The huge flexibility in synthesizing light-harvesting semiconducting molecules[6] can be exploited to match their main absorption bands with the emission spectra of various indoor light sources, thereby minimizing thermalization and transparency losses that would otherwise reduce the power conversion efficiency (PCE).[7] As a result, their optical bandgap can be set at the optimum for indoor photovoltaics (1.9–2.0 eV)[1] and their PCE surpass that of inorganic photovoltaic technologies, such as hydrogen-passivated amorphous silicon (which shows a bandgap of 1.6 eV[2] and reported PCEs of 19–21% at 1000 lux and under cool light-emitting diode (LED) illumination).[8] Research on indoor OPV materials and devices has led to impressive PCEs beyond 30% (at 2000 lux, warm LED)[9–11] while some of the challenges related with their industrialization

X. Rodríguez-Martínez, S. Riera-Galindo, G. Beket, F. Gao, O. Inganäs
Biomolecular and Organic Electronics
Department of Physics, Chemistry and Biology
Linköping University
SE 581 83 Linköping, Sweden
E-mail: correspondence@xabirodriguez.com

The ORCID identification number(s) for the author(s) of this article can be found under https://doi.org/10.1002/adfm.202301192.

DOI: 10.1002/adfm.202301192

P. Hartnagel, T. Kirchartz
IEK-5 Photovoltaics
Forschungszentrum Jülich GmbH
52425, Jülich, Germany

G. Beket, T. Österberg
Epishine AB
Wahlbecksgatan 25, SE 582 13 Linköping, Sweden

T. Kirchartz
Faculty of Engineering and CENIDE
University of Duisburg-Essen
Carl-Benz-Str. 199 47057, Duisburg, Germany

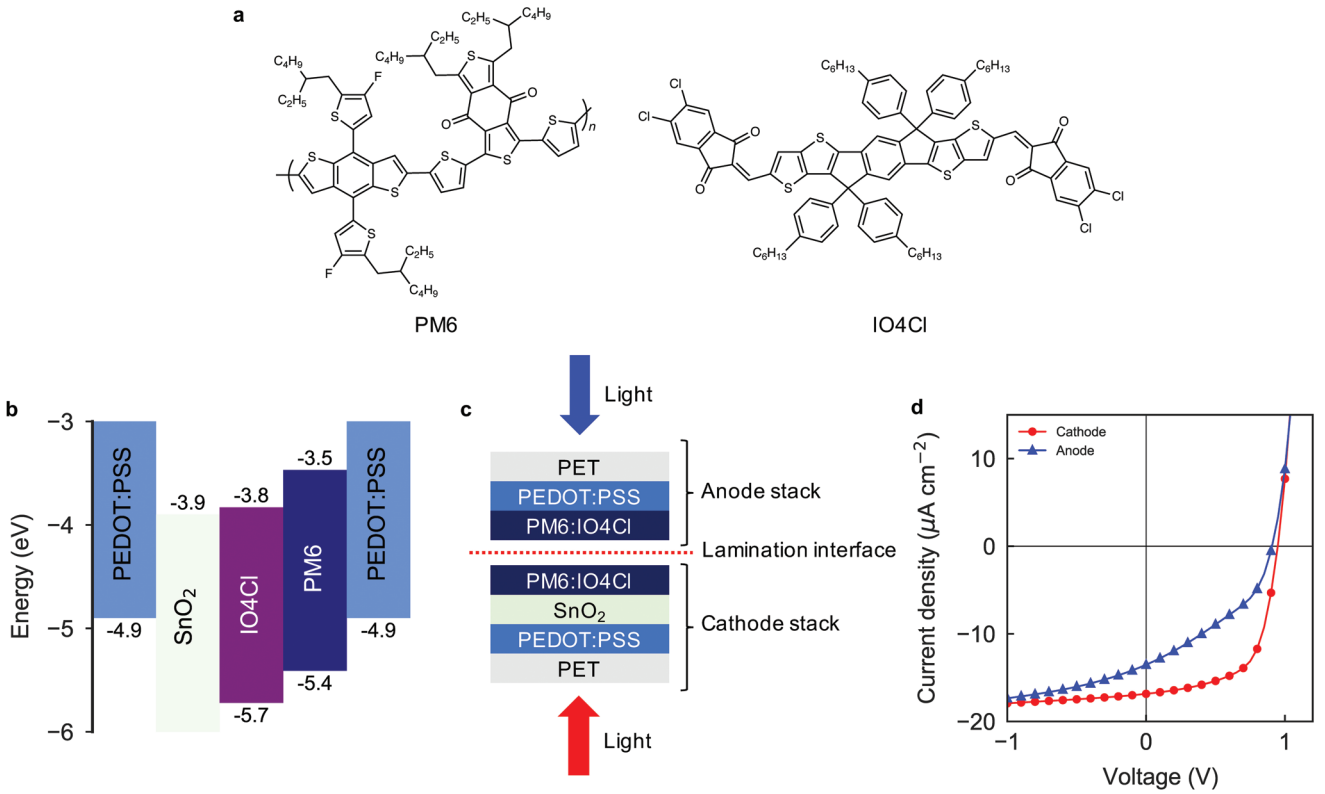

Figure 1. a) Molecular structures of the PM6 donor polymer and IO4Cl small molecule acceptor. b) Energy diagram representing the frontier energy levels of the layers forming the functional device stack. The energy levels represented correspond to either the work functions of the PEDOT:PSS PH1000 contacts and SnO_2 (obtained from the commercial supplier) or the HOMO and LUMO energy levels of PM6 and IO4Cl.[10] c) Cross-sectional cartoon of a laminated device, with the lamination interface (dotted red line) set in between the bulk heterojunction (BHJ) layers. Depending on the side of light incidence, we differentiate cathode (red arrow) and anode (blue arrow) side illumination conditions. d) Typical *J–V* curves for cathode and anode side illumination (545 lux) of a 200 nm thick blade coated PM6:IO4Cl device in air.

(e.g., air-processability and photoactive layer (PAL) thickness tolerance) are also being intensively investigated.[12] Compared to lead-halide perovskites, OPVs offer improved environmental sustainability as being naturally free of lead or iodide ions, which are known to constitute a biological risk and a safety threat when in close contact with living organisms (such as in indoor environments).[13–15] Substantial efforts are focused on formulating lead-free perovskites,[16] yet so far showing limited light absorption, PCE (<13% under 1 sun) and lifetimes.[1,17]

As indoor irradiances (≈3 W m^{-2} at 1000 lux in an office environment) are typically three orders of magnitude below outdoor conditions (1 sun or 1000 W m^{-2}), an essential requirement of high-performing indoor OPV devices is to maximize the open-circuit voltage (V_{oc}), which depends logarithmically on light intensity.[18,19] Recently, a wide bandgap non-fullerene acceptor (NFA) termed as IO4Cl (3,9-bis[5,6-dichloro-1H-indene-1,3(2H) dione]-5,5,11,11-tetrakis(4-hexylphenyl)-dithieno[2,3-*d*:2′,3′-*d*′]-s-indaceno[1,2-*b*:5,6-*b*′]dithiophene, shown in **Figure 1**a) was especially designed to have excellent spectral overlap with indoor light sources.[10] Cui et al. reported opaque *p–i–n*, blade coated and evaporated OPV devices with V_{oc} values exceeding 1 V under 200 lux and PCEs >26% under 1000 lux when blending IO4Cl with the workhorse donor polymer PM6 (poly[(2,6-(4,8-bis(5-(2-ethylhexyl-3-fluoro)thiophen-2-yl)-benzo[1,2-*b*:4,5-*b*′] dithiophene))-*alt*-(5,5-(1′,3′-di-2-thienyl-5′,7′-bis(2-ethylhexyl) benzo[1′,2′-*c*:4′,5′-*c*′]dithiophene-4,8-dione)], Figure 1a), which constituted a breakthrough in the indoor OPV field. Other material families, such as that represented by benzotriazole (BTA)-based wide bandgap NFAs,[20] are equally promising for indoor OPV applications with reported PCE values surpassing 28% under 1000 lux and over large areas (1 cm^2).[21–23] However, beyond demonstrating promising performance on a laboratory scale and by fabrication in inert environments, the successful commercialization of certain PAL -such as PM6:IO4Cl- in R2R manufacturing scenarios poses additional requirements beyond PCE.[24] These include, among others, i) processability in air[25]; ii) high performance at large PAL thicknesses[26]; iii) tolerance upon unintentional variations of thickness[26]; and iv) compatibility with inverted (*n–i–p*) device architectures, which are certainly not fulfilled by all donor:acceptor blends. It is often considered that lacking at least one of these features is enough to diminish the industrial interest of certain OPV blend.[24]

The manufacturing of OPV cells by lamination is receiving attention as a high-throughput and scalable approach compatible with R2R.[12,27–29] Therein, two independent and flexible multi-layered stacks are brought and held together using the PAL as adhesive with the help of two warm counter-rotating rolls, thus rendering a fully functional device. There are several advantages of this approach for indoor OPV. By lamination most of the shunting pathways (such as pinholes, defects)

derived from solution processing are largely mitigated, thus significantly increasing the shunt or parallel resistance of the devices. This fact notably reduces the dark current at low forward bias, enabling high V_{oc} and fill factor (FF) values at low light intensities.[19,30–32] Nevertheless, when both substrates and electrodes are highly transparent (e.g., using polyethylene terephthalate (PET) foils and poly(3,4-ethylenedioxy thiophene):poly(styrenesulfonate) (PEDOT:PSS) electrodes), the functional devices become semitransparent and might show different performance depending on the illumination side.[29,33] The effect extends beyond their intrinsic optical asymmetry due to the electron transport layer (ETL) and the hole transport layer (HTL), which makes the illumination sides strictly non-equivalent even when using PEDOT:PSS as electrode on both stacks. As reported by Bergqvist et al.,[29] an asymmetric photocurrent extraction builds-up in laminated poly(2,3-bis-(3-octyloxyphenyl)quinoxaline-5,8-diyl-*alt*-thiophene-2,5-diyl):[6,6]-phenyl-C_{71}-butyric acid methyl ester (TQ1:$PC_{71}BM$) blends as a function of exposure time to ambient, with the anode side performance being generally worse than that of the cathode side. The researchers associated the phenomenon to a significant electron trap density on the anode side PAL after exposure to ambient, as evidenced from optical modeling, mobility data, and light-dependent recombination analysis. Whether high-performing NFA-based blends could overcome, or not, the so far reported limitations of laminated fullerene-based blends is an open yet important question to address, namely, to advance the PCE of indoor OPV devices to unprecedented levels with larger industrial interest.

Here we investigate the potential of the high V_{oc} PM6:IO4Cl blend for its adoption onto R2R-compatible devices, namely indoor OPV cells processed entirely in air by blade and slot-die coating and based on the lamination concept. In these devices, external quantum efficiency (EQE) measurements combined with drift-diffusion and optical simulations indicate that an anomalous layer that does not contribute to the photocurrent forms precisely at the PAL/anode contact interface. For thicker PALs (>100 nm), such a layer creates an undesired asymmetry in the device photocurrent and *J–V* curve depending on the illumination side. We observe that by fabricating solar cells with asymmetric PAL thicknesses or, alternatively, by placing the lamination interface closer to the PAL/anode contact interface, the electrical asymmetry is partly mitigated. In the limit where both cathode and anode side PALs are thin enough (<35 nm each), the *J–V* curve symmetry is almost completely restored at the expense of lower PCE due to the reduction in photoactive volume. Hence, whenever cathode/anode electrical parity is required, PM6:IO4Cl devices must be very thin, which imposes limitations to their up-scaling by R2R methods. By transferring the device prototyping and characterization steps to inert atmosphere, we observe that the photocurrent asymmetry does still arise. In these conditions and by extending the study to several donor:acceptor blends, we associate the photocurrent asymmetry to a morphological and/or vertical phase segregation issue rather than to an electron trap density increase at the anode side. Interestingly, we identify at least two binary blends, namely an all-polymer and a polymer:fullerene blend, that show good electrical symmetry even on thick devices (yet by spin coating in a nitrogen-filled glovebox). A ternary blend where a fullerene is added onto the PM6:IO4Cl binary is also identified as a potential way to mitigate the photocurrent asymmetry of thick devices, thus opening further research routes in the future.

2. Results and Discussion

2.1. Archetypal PM6:IO4Cl *J–V* Curves and Possible Sources of Their Asymmetry

The molecular structures of the donor polymer PM6 and the small molecular acceptor IO4Cl are depicted in Figure 1a. Figure 1b shows the energy diagram of an OPV device, including PM6:IO4Cl as PAL, PEDOT:PSS as electrodes, and SnO_2 as ETL. SnO_2 is selected as ETL due to its superior indoor performance and the unnecessary UV photoactivation compared to ZnO formulations.[12] Figure 1c shows a cross-sectional cartoon of that same laminated device. In this case, two independent PET substrates coated with PEDOT:PSS as electrodes are brought together at the PAL interface, with the cathode side stack including the required ETL. At the anode side stack, PEDOT:PSS has dual functionality (HTL and electrode). These devices are semitransparent and might show distinct *J–V* characteristics depending on the illumination side (Figure 1d). For thick blade-coated PM6:IO4Cl devices in air (with the PALs coated at 15 mm s^{-1}), the photovoltaic figures-of-merit upon cathode side illumination (red circles in Figure 1d, yielding V_{oc} = 0.95 V, short circuit current density (J_{sc}) = 16.8 μA cm^{-2}, FF = 61.7%, and PCE = 6.6% under 545 lux) outperform the anode side counterparts (V_{oc} = 0.91 V, J_{sc} = 13.5 μA cm^{-2}, FF = 38.4%, and PCE = 3.2%). The irradiance of the cool LED light source used in this work is shown in Figure S1 (Supporting Information). For the device shown in Figure 1d, a film thickness of ≈100 nm is expected per PAL (Figure S2a, Supporting Information), thus making up a total of ≈200 nm after lamination. The PAL thicknesses are determined by fitting visible transmittance data while using the previously acquired complex refractive indices (Figure S3, Supporting Information) and assuming loss of coherence through the thick (125 μm) PET substrate. Furthermore, we assure that in our experiments, light traverses only once the device stack, as expected for semitransparent devices without any back reflectors, which also explains part of the observed drop in J_{sc} compared to previous reports[10] using opaque devices. This is guaranteed by placing the OPV devices on top of a black background (anti-reflective) during the acquisition of the *J–V* curves, in agreement with a recently introduced catalog of good practices for the characterization of semitransparent OPV cells.[34]

Upon anode side illumination (blue triangles in Figure 1d), the *J–V* curve shows a pronounced *kink* that indicates increased field dependence for charge extraction. This implies that photogenerated charges are harder to separate and collect at the electrodes when light impinges from the anode side of the device. Note that as per transfer matrix modeling, the intrinsic optical asymmetry (attributed to the ETL on the cathode side compared to the anode stack) does not quantitatively explain the observed decrease in J_{sc} upon different illumination side; in this case, the current density expected is virtually identical

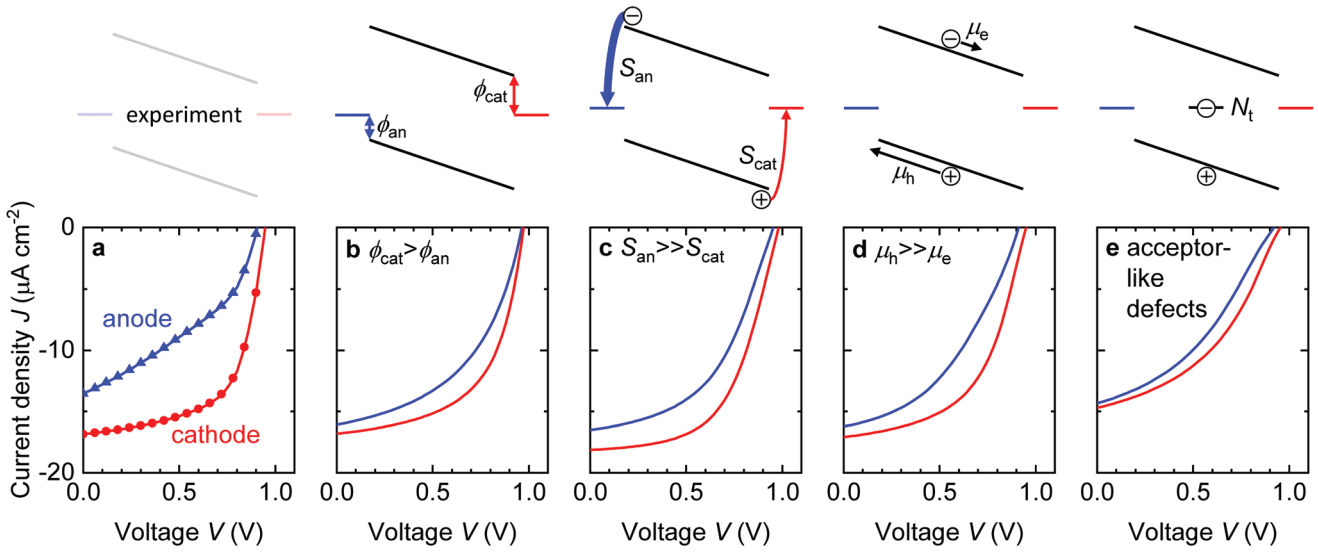

Figure 2. Drift-diffusion simulations reveal possible sources of the *J–V* curve asymmetry in the a) experimental *J–V* characteristics between anode side illumination (blue triangles) and cathode side illumination (red circles) of a semitransparent OPV cell with a thick active layer of 200 nm. The *J–V* curves in the case of b) asymmetric injection barriers ($\phi_{cat} > \phi_{an}$) can explain the experimental observation, but also c) asymmetric surface recombination ($S_{an} >> S_{cat}$), d) asymmetric charge-carrier mobilities ($\mu_h >> \mu_e$) and e) acceptor-like trap states (with a density of states N_t) can all cause the photovoltaic cell to perform worse upon anode side illumination.

(50.9 and 51.0 μA cm^{-2} for cathode and anode side illumination, respectively, as per the EQE integration in Figure S4, Supporting Information). These values are, however, more than three-fold higher than what we observe experimentally (16.8 and 13.5 μA cm^{-2} for cathode and anode side illumination, respectively), hence ruling out the device semitransparency as the origin of the photocurrent loss. Transport and recombination losses of free charge carriers are neither a plausible cause as FF values are decent (up to 61.7% for cathode side illumination). We therefore suggest that the PM6:IO4Cl blend in this specific device structure has issues with the separation of generated excitons into free charges, or loss of excitons because of charge-induced quenching.[35] On the other hand, the asymmetry in performance between illumination directions could be a purely electrical effect caused by asymmetric properties throughout the bulk of the PAL, or an indication for differences between the anode and cathode side PALs. Accordingly, we first investigate the influence of electrical properties on the asymmetric device performance before moving to an analysis of the influence of the device architecture.

Figure 2 presents the different sources that might cause the discrepancy in the performance between anode and cathode side illumination observed experimentally (Figure 2a). For this discussion, we use drift-diffusion simulations (with an exciton dissociation efficiency of 0.4) of a semitransparent OPV cell. We accordingly explore the influence of different electronic properties in a systematic manner. For details and simulation parameters, we refer to the Experimental Section and Tables S1 and S2 (Supporting Information). First, we set the injection barriers (ϕ) asymmetrically since the frontier energy levels in Figure 1b indicate a difference between cathode and anode contacts. In Figure 2b, we observe that such asymmetric contact barriers ($\phi_{cat} > \phi_{an}$) can, in fact, cause an asymmetry in the *J–V* curves between illumination direction. However, Figure 1b indicates energy levels that would support the opposite trend. Even for symmetric contacts ($\phi_{cat} = \phi_{an}$), when increasing the recombination rate (S) of electrons at the anode while assuming a selective contact at the cathode ($S_{an} >> S_{cat}$), we observe a splitting of the simulated *J–V* curves in Figure 2c. The reason is that when illuminating the device from its anode side, the electron density at the anode is higher than for cathode side illumination. Therefore, more charge carriers are lost due to surface recombination at the anode leading to an asymmetric degradation of the *J–V* characteristics. Similarly, dissimilar charge-carrier mobilities (μ) can cause such behavior as demonstrated in Figure 2d. For each illumination direction, the μ of the carrier type that must travel to the opposite contact is relevant. Hence, for anode side illumination, the electron mobility (μ_e) is more relevant since holes can readily be extracted at the anode. Therefore, when the hole mobility (μ_h) is higher than μ_e ($\mu_h >> \mu_e$), more charge carriers are extracted for the cathode side illumination than for the anode side illumination. These effects could be even enhanced if μ values were not constant as assumed in the drift-diffusion simulations. It has been observed that in OPV charge carriers might not be fully thermalized when being extracted.[36] Different cooling rates between electrons and holes could therefore cause a change in μ ratio depending on illumination direction. Lastly, introducing trap states (quantified with a density of states N_t) into the system can cause space-charge effects due to the charge of the trap. Figure 2e shows that acceptor-like defects will also cause slightly different shapes in the *J–V* curves. Therefore, we have demonstrated that even in a very simple device model, several different properties can evoke asymmetric *J–V* curves upon changing the illumination direction. However, this generic set of simulation parameters was not able to replicate the specific shape of the experimental data, in particular the difference in FF values. So, for correct interpretation of the data, it is on the one hand hard to identify the

dominant source of asymmetry or a combination of multiple effects. On the other hand, due to the special processing conditions of laminating two PALs on top of each other, a simple device model with constant properties throughout the laminated layers might be insufficient. In the following, we therefore systematically investigate the influence of the position of the lamination interface and the different PAL thicknesses on *J*–*V* curve asymmetry.

2.2. Moving the Lamination Interface through the PAL

We first investigate how the location of the lamination interface affects the *J*–*V* characteristics. To make a rapid qualitative assessment of the experimental conditions (if any) that mitigate the *J*–*V* curve asymmetry, we exploit antiparallel PAL thickness gradients prepared by blade coating, so that the overall PAL thickness remains approximately constant as schematically depicted in **Figure 3**a. Such arrangement serves us to study the influence of the position of the lamination interface on the device performance while using minimal fractions of time and resources. Experimentally, we first slot-die coat an array of eight PEDOT:PSS contacts to then blade coat the ETL and the PAL orthogonally to the formers. PAL thickness gradients are generated by ink depletion at the blade ink reservoir, i.e., by reducing the blade-to-substrate gap to <50 µm, pipetting very limited volume (20–30 µL) and using relatively high coating speeds (40–50 mm s^{-1}). These processing conditions together with the use of wide PET substrates (25 mm) lead to the desired PAL thickness gradient along the coating direction. Importantly, the processing keeps good homogeneity along the short axis and bypasses the need for blade acceleration/deceleration,[37,38] which is a feature unavailable in most commercial blade coating setups. By inspecting the *J*–*V* curves of the eight different pixels (Figure 3b) we observe that: i) the performance under cathode side illumination outperforms anode side illumination in all cases; and ii) both the anode and cathode side *J*–*V* curves characteristics progressively improve as the lamination

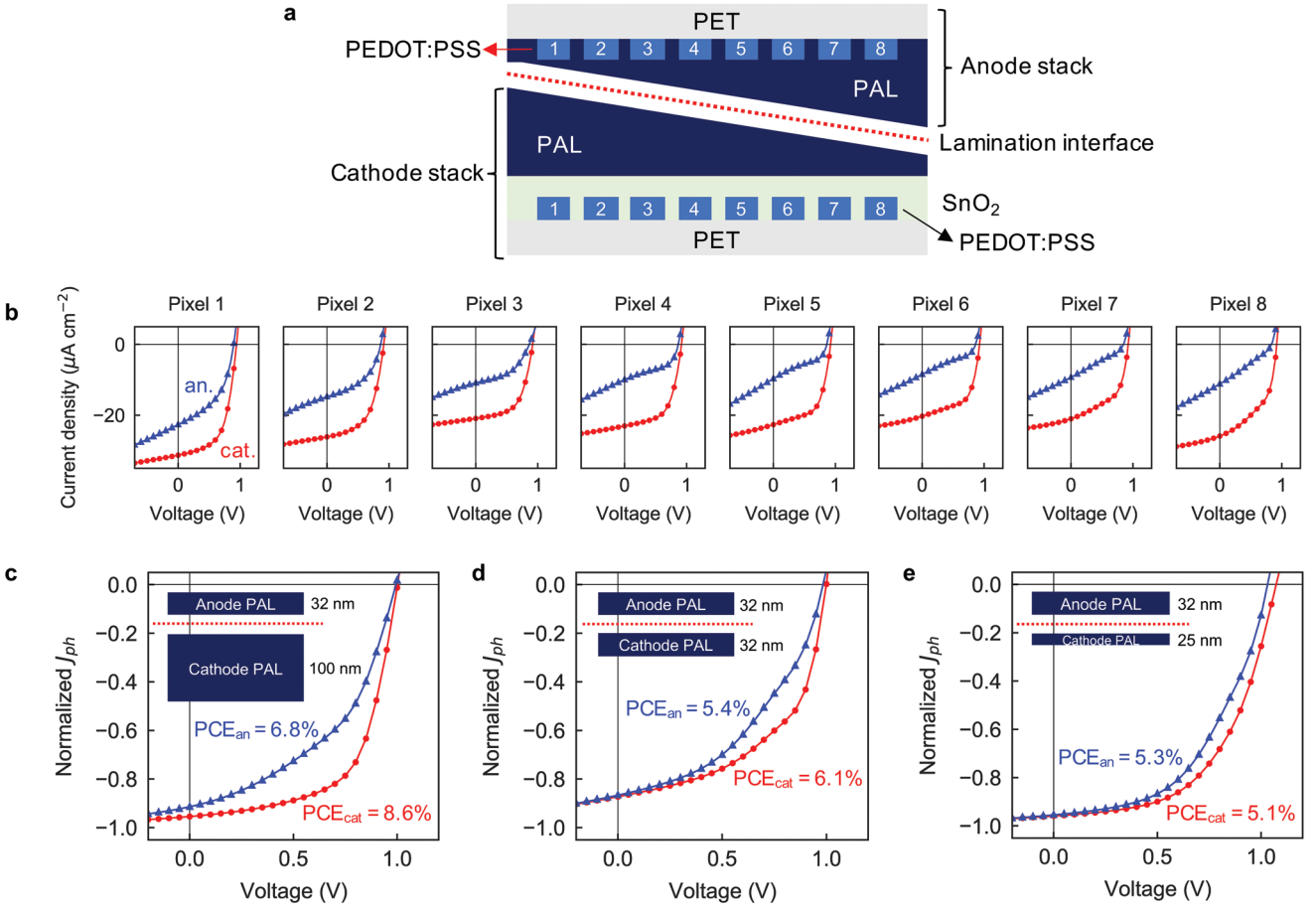

Figure 3. a) High-throughput evaluation of the influence of the lamination interface position on device performance. The PALs are deposited by blade coating to create lateral thickness gradients. Then, they are positioned in an antiparallel fashion to linearly vary the position of the lamination interface with respect to the other device interfaces. As a result, the overall PAL thickness remains approximately constant along the lamination interface gradient direction at ≈150 nm. Note that an array of eight PEDOT:PSS contact lines is previously slot-die coated perpendicularly to the PAL lamination interface gradient direction, thus screening eight different devices (pixels) in a single substrate. b) The corresponding *J*–*V* curves of the eight pixels acquired at 545 lux, for cathode (red circles) and anode (blue triangles) side illumination conditions. Normalized J_{ph}–*V* curves of homogeneous laminated devices with their anode side PAL blade coated at 5 mm s^{-1} (32 nm thick) and the cathode side PAL blade coated at c) 15 mm s^{-1} (100 nm thick), d) 5 mm s^{-1}, and e) 2.5 mm s^{-1} (25 nm thick).

interface is set farther from the PAL/ETL interface at constant overall PAL thickness (see the corresponding PCE trends in Figure S5d, Supporting Information). Therefore, our results have two complementary practical interpretations: i) setting the lamination interface the farthest from the PAL/ETL interface (i.e., pixel 1) and ii) using a thinner anode side PAL could be exploited to improve the device performance and mitigate the cathode/anode side *J–V* curve asymmetry.

Following these observations, we further compare the performance of homogeneously blade-coated laminated devices featuring a thin anode PAL (5 mm s^{-1}/32 nm) and a cathode PAL of variable thickness (15, 5, or 2.5 mm s^{-1}, corresponding to 100, 32, or 25 nm, respectively, Figure S2, Supporting Information). Note that the anode side PAL could not be made thinner (such as 2.5 mm s^{-1}) to guarantee proper lamination and device function. The normalized J_{ph}–*V* curves shown in Figure 3c–e complement very well our previous observations. The *J–V* curve normalization is performed by computing the ratio between J_{ph} ($J_{ph} = J–J_{dark}$, with J_{dark} corresponding to the current density in the dark) and J_{ph} under reverse bias (–1 V, $J_{ph,sat}$) as a way to illustrate better the corresponding *J–V* curve symmetry (the raw *J–V* curves are accordingly shown in Figure S6, Supporting Information). We notice that despite keeping a thin anode PAL improves the photovoltaic performance, using a thick cathode PAL (100 nm, Figure 3c) introduces a larger cathode/anode asymmetry at the expense of providing better absolute PCE figures (8.6% and 6.8% for cathode and anode sides, respectively). Conversely, when thinner cathode PALs are employed, the overall PCE drops yet the cathode/anode symmetry is improved. This fact is illustrated in Figure 3d, where a device featuring a 32 nm thick cathode layer shows 6.1% and 5.4% PCE for the cathode and anode sides, respectively; and Figure 3e, where a device, including a 25 nm thick cathode layer shows 5.1% and 5.3% PCE for cathode and anode side illumination, respectively. Thus, it is only when both thin anode and cathode PALs are employed that their *J–V* curves become more symmetric; yet with limited PCE due to the reduced volume of photoactive material available. That is precisely pointing out the existence of a trade-off between absolute PCE and cathode/anode symmetry in air-processed, laminated PM6:IO4Cl devices. In those scenarios where cathode/anode symmetry is not a must, devices featuring a thin anode layer and a thick cathode layer show the best absolute PCE when illuminated from the cathode side only. Nonetheless, symmetric *J–V* curves are obtained in thin devices (<35 nm per PAL) at the expense of lower PCE.

On the other hand, the light utilization efficiency (LUE), which is defined as the product of PCE and average photopic transmittance (APT, Figure S7, Supporting Information),[39] increases as the devices become thinner. Particularly, for the thicker device shown in Figure 3c, the LUE for the cathode and anode sides reads 0.97% and 0.77%, respectively, whereas for the thinner device (Figure 3e), the LUE increases up to 0.99% and 1.03% for the cathode and anode sides, respectively. This is a relevant outcome that motivates the use of thinner PALs when searching for an improved trade-off between device semitransparency and performance, as well as proper cathode/anode electrical symmetry. In this work, we did not simultaneously achieve both higher PCEs (>10%) and proper cathode/anode symmetry for blade-coated PM6:IO4Cl devices in air.

2.3. Light Intensity-Dependent Recombination Analysis

The device physics behind the cathode/anode asymmetry in PM6:IO4Cl devices is further investigated by light intensity-dependent recombination analysis of two archetypal devices, featuring either asymmetric (Figure 1d) or symmetric (Figure 3e) *J–V* curves. The electrically asymmetric device consists of two thick PALs deposited at 15 mm s^{-1} (100 nm) each (see inset of **Figure 4**c), whereas the symmetric device consists of thinner PALs deposited at 2.5 (25 nm) and 5 mm s^{-1} (32 nm), on the cathode and anode sides, respectively (see inset of Figure 4g). The light ideality factor (n_{id}) obtained by fitting V_{oc} as a function of illuminance (Φ) on the thick device as[40]

$$n_{id} = \frac{q}{k_B T} \frac{dV_{oc}}{d \ln \Phi} \quad (1)$$

is 1.57 ± 0.02 and 1.67 ± 0.09 for cathode and anode side illumination, respectively, with k_B the Boltzmann's constant, T the absolute temperature, and q the elementary charge. A brief mathematical derivation and common misconceptions on the use of Equation 1 are detailed in Note S1 (Supporting Information). Ideality factors ≈1.6 suggest that recombination is mainly via localized states within the bandgap. As n_{id} is significantly <2, the states are either not in the middle of the bandgap or the carrier concentrations are not equal where the recombination rate is high.[41,42] The latter case could be caused by electrical asymmetries as discussed in Figure 2. We also observe that the cathode side V_{oc} is systematically ≈50 mV higher compared to the anode side V_{oc} (Figure 4a). The α exponent that fits the $J_{sc} \propto \Phi^{\alpha}$ relationship[43] in Figure 4b is also higher when the thick device is illuminated from the cathode side (0.993 ± 0.001 and 0.975 ± 0.005 for cathode and anode, respectively), which indicates that bimolecular recombination and space-charge are more likely in short circuit conditions when the device is illuminated from the anode side.[43,44] There is, then, a severe recombination pathway on the anode side of the thick device, which is further confirmed when depicting the FF as a function of Φ. The FF shows the largest discrepancy between cathode and anode, as shown in Figure 4c. FF values under cathode side illumination reach 66%, whereas they never exceed 40% when the device is illuminated from the anode side. Interestingly, the corresponding EQE measurements of the thick device show distinctive features for cathode and anode side illumination conditions (Figure 4d). The cathode side EQE is systematically higher than the anode side counterpart, thus matching the experimental observation in terms of (integrated, J_{EQE}) J_{sc} (Figure 4b). Furthermore, the anode side EQE spectrum shows a deep and characteristic bimodal valley at ≈600 nm. This is an unexpected feature given the extinction coefficient of the PAL (Figure S3b, Supporting Information) and the EQE spectra reported elsewhere.[10]

The light intensity-dependent recombination analysis of the thinner device generally shows improved matching between cathode and anode side characteristics. V_{oc} values are closer and apparently offset-free, with the corresponding n_{id} reading 1.93 ± 0.07 and 2.1 ± 0.2 for cathode and anode sides, respectively (Figure 4e). In this case, ideality factors ≈2 are indicative of recombination via deep (mid-gap) states,[41,45] which apparently

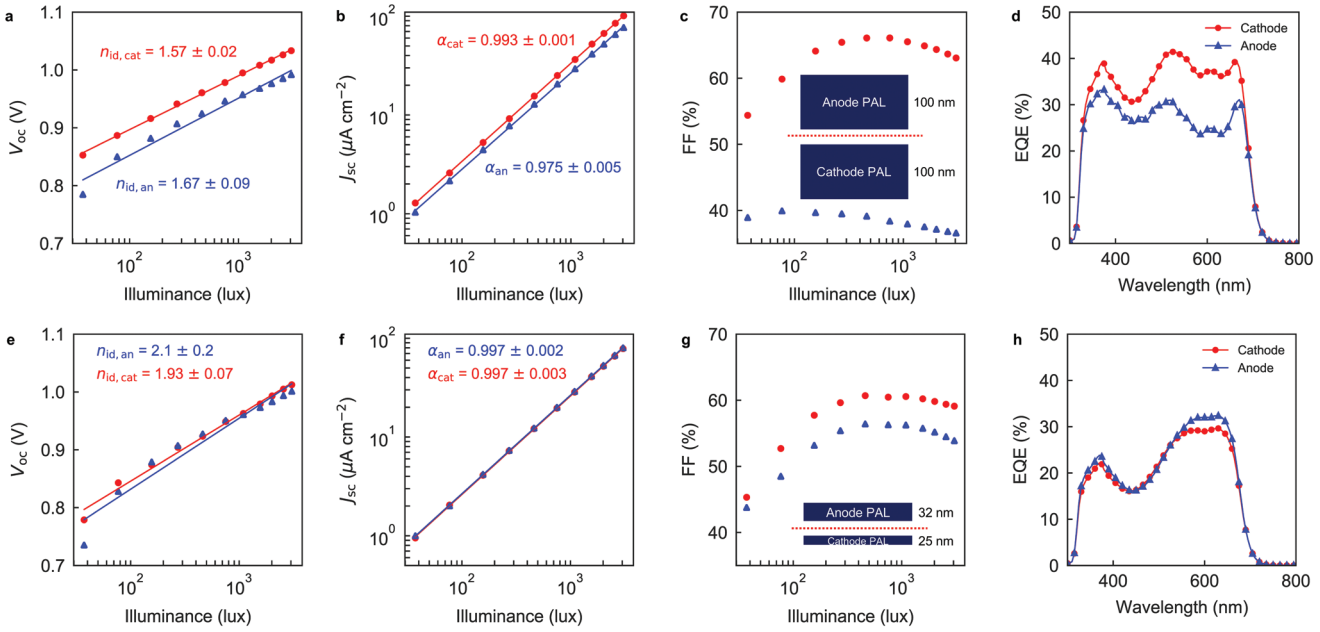

Figure 4. Light intensity-dependent recombination analysis of the photovoltaic performance and EQE spectra of two archetypal PM6:IO4Cl laminated devices. For a thick device where PALs are 100 nm thick each (see inset in (c)), we show the a) V_{oc}, b) J_{sc}, and c) FF as a function of illuminance (Φ). d) EQE spectrum of that same thick device, for cathode (red circles) and anode (blue triangles) side illumination. e) V_{oc}, f) J_{sc}, and g) FF of a thinner laminated device where the cathode and anode side PALs are 25 and 32 nm thick, respectively (see inset in (g)). h) EQE spectrum of the thin device for cathode and anode side illumination.

constitute the main recombination mechanism in thin devices. Moreover, J_{sc} values are virtually identical and α values read 0.997 ± 0.003 and 0.997 ± 0.002 for cathode and anode sides, respectively (Figure 4f). FF values are moderately high, with maxima of ≈60% and 56% for cathode and anode sides, respectively (Figure 4g). The corresponding EQEs (Figure 4h) are mostly overlapping and their spectral shape is within our expectations based on the extinction coefficient of the PAL (Figure S3b, Supporting Information) and optical modeling of an *ideal* laminated device (Figure S4, Supporting Information). Importantly, the characteristic drop in the EQE at ≈600 nm observed on the thick device is herein absent.

2.4. Spectral Analysis and Modeling of Photocurrent: Filtering Layers Introduce *J–V* Curve Asymmetry

Reverse-biased EQE spectra provide further insights about the origin of the cathode/anode asymmetry in thick laminated PM6:IO4Cl devices. Our investigation starts by transferring the most critical fabrication steps, namely the PAL deposition and lamination, to a nitrogen-filled glovebox, which serves us to discard potential device artifacts assigned to degradation or trap-assisted recombination derived from oxygen and light exposure.[25] As a blade coater cannot be fitted in our glovebox, in these exploratory experiments we spin coat the PALs to obtain ≈75 nm thick layers (each). We proceed with the lamination and *J–V* curve acquisition in the glovebox followed by a rapid transfer to air to obtain the EQE spectra shown in **Figure 5**a,b for anode and cathode side illumination conditions, respectively, at short circuit (0 V) and under reverse bias (–5 V). The unbiased EQE spectra indicate that a severe (integrated) J_{EQE} asymmetry exists, reading 20.2 and 13.2 μA cm^{-2} for the cathode and anode sides, respectively. From the corresponding *J–V* curves (Figure S8, Supporting Information), J_{sc} reads 20.9 and 18.8 μA cm^{-2} for the cathode and anode sides, respectively, thus indicating a large discrepancy on the anode side between J_{EQE} and J_{sc}. This discrepancy could be ascribed to the *s*-shape of the *J–V* curve or to extended degradation on the anode BHJ layer upon air exposure (as required for EQE acquisition). Under reverse bias, we observe an increase in the EQE for both illumination directions, but most significantly for anode side illumination. Therefore, the strong reverse bias revokes the asymmetry and causes similar J_{EQE} values.

When examining its spectral shape, the EQE measured at 0 V with illumination from the anode shows severe losses in the wavelength range between 500 and 700 nm (Figure 5a), similar to our observation in Figure 4d for a thicker (200 nm) blade coated device in air. Under reverse bias (–5 V, Figure 5a), the three local maxima initially shown (500–700 nm) are no longer present, hence the EQE resembles that for cathode side illumination under identical bias conditions (Figure 5b). Optical modeling of the EQE in Figure S4 (Supporting Information), reveals that the features observed at short circuit when illuminated from the anode side (Figure 5a) cannot be replicated by the optical constants of the blend. Also, Figure S4 (Supporting Information), illustrates that the EQE remains constant over a wide range of incoming photon fluxes. Thereby, we can rule out that the local maxima are caused by the light source of the EQE setup varying in intensity for different wavelengths.

We continue our investigation by modeling the generation rate as a function of wavelength and position in the PAL for

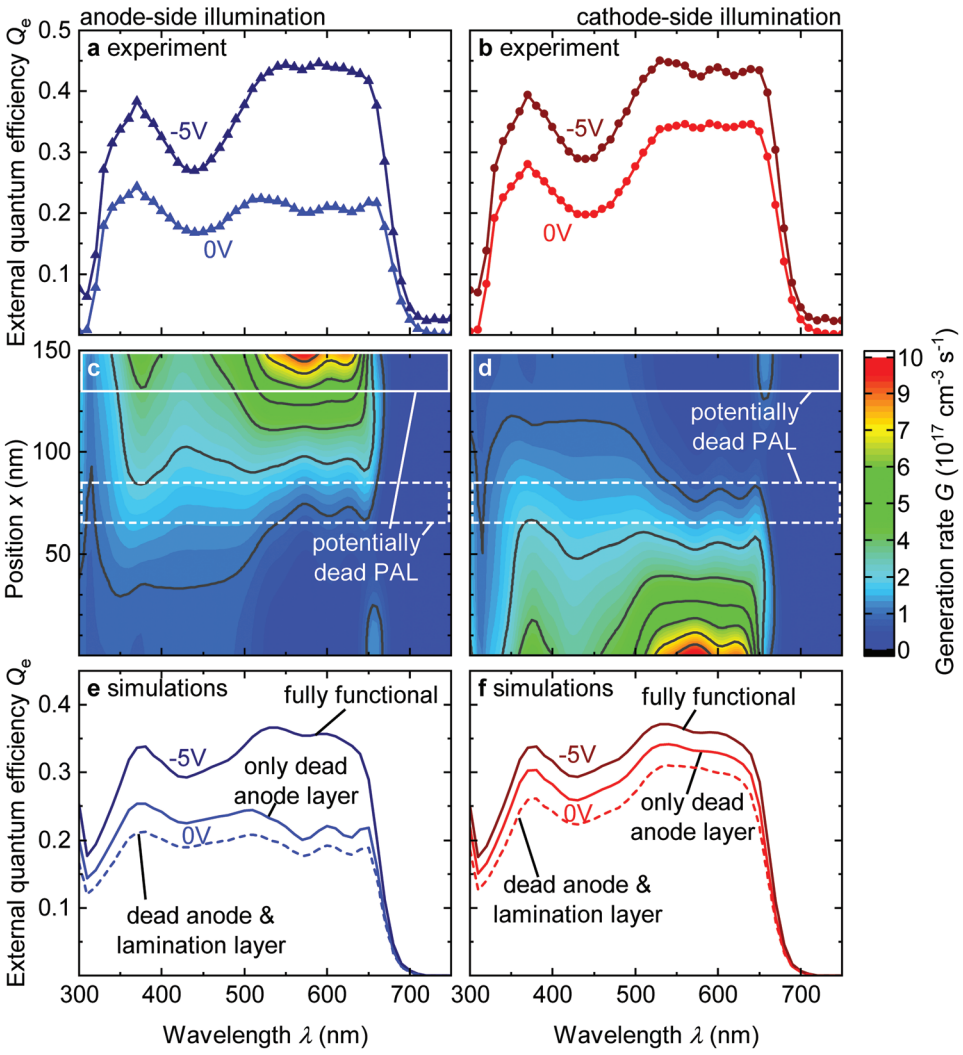

Figure 5. Experimental EQE measurements under a) anode side illumination and b) cathode side illumination at short circuit ($V = 0$ V) and under strong reverse bias ($V = -5$ V) for a 150 nm thick PAL that was fabricated under inert conditions. Generation rate G as a function of wavelength λ and position x in the active layer for c) anode side illumination and d) cathode side illumination simulated for a device with a well-functioning 150 nm thick PAL. At the anode (solid white rectangle) and at the lamination interface (dashed white rectangle), we remark PAL fractions that (potentially) do not contribute to the photocurrent. e,f) Simulated EQE spectra. Solid lines at 0 V correspond to device model 1, which assumes a dead PAL region of 20 nm at the interface with the anode contact (PEDOT:PSS). In such a dead layer, no excitons are dissociated at short circuit, yet they do and with the same efficiency as in the remaining PAL (0.5 is assumed) under reverse bias (−5 V, rendering the PAL fully functional). Dashed lines at 0 V correspond to the simulated EQE according to device model 2, which includes an additional dead PAL at the lamination interface. Both device models can explain the difference between cathode and anode side illumination at short circuit while the similarity of the EQE at reverse bias points toward a voltage-dependent exciton dissociation efficiency in the dead regions. However, as demonstrated in Note S2 (Supporting Information), the lamination interface leaves no indication of degraded photovoltaic performance.

anode and cathode side illumination (Figure 5c,d, respectively). Most of the generation takes place in the first 50 nm from the illuminated interface with a maximum between wavelengths of 550 and 600 nm. This regime coincides with the wavelength interval at which the experimental EQE from the anode side is significantly below that from the cathode side. Also, the generation rate in the middle of the PAL shows distinct local maxima between 500 and 650 nm that resemble the anode side EQE in short circuit (c.f. Figure 5a,c,d). Therefore, we hypothesize that a fraction of the PAL near the anode contact (precisely at the PEDOT:PSS/PAL interface) absorbs light without contributing to the photocurrent, as it was suggested by Bergqvist et al. to occur in fullerene-based laminated OPV devices.[29] This results in a filtering effect when the OPV cell is illuminated from the anode side yet having virtually no impact upon cathode side illumination. As the laminated PM6:IO4Cl PAL used so far in this work already features issues with exciton separation (Figure S9, Supporting Information), such a problem might be amplified closer to the anode contact.

To test this hypothesis, we include in our simulations a 20 nm thick layer at the PEDOT:PSS/PAL interface (Figure S10b, Supporting Information), which only participates in absorption and transport, but not in charge-carrier generation. Figure S11 (Supporting Information), depicts the corresponding thickness

screening study (5–25 nm thicknesses) resulting in 20 nm as the best fit to our experimental data. Thereby, we set a null exciton-dissociation efficiency in the dead PAL region, which corresponds to the areas marked with solid white rectangles in Figure 5c,d. As per this device model, the simulated anode side EQE under 0 V (Figure 5e) shows the same features as the experimental data (Figure 5a). On the other hand, the simulated cathode side EQE (Figure 5f) remains significantly higher and unaffected by the dead layer at the anode side, where generation is low anyhow. We further explore the possibility for the PAL around the lamination interface to show negligible exciton-dissociation efficiency, as this is found to negatively affect the EQE spectra (dashed lines in Figure 5e,f). These potentially dead regions would correspond to the areas marked with dashed white rectangles in Figure 5c,d. However, as we demonstrate in Note S2 (Supporting Information), a comparison of experimental and simulated *J–V* curves in both scenarios considered (i.e., 1 or 2 dead layers, corresponding to model 1 and model 2, respectively, Figure S10, Supporting Information) leaves no indications that either anomalous exciton-dissociation or filtering issues arise at the lamination interface.

We emphasize that further experiments are needed to verify or falsify the hypothesis of weak exciton dissociation at the PAL fraction nearby the anode contact. A filtering effect can also be observed if charge-carrier generation is intact, but the free charge-carriers cannot be extracted, for example, due to decreased μ values in the dead PAL (Figure S12, Supporting Information). Particularly, air processing is found to negatively affect electron transport in PM6:IO4Cl blends as evidenced by hole and electron mobility data of single-carrier devices working in the space-charge limited current (SCLC) regime (Figure S13, Supporting Information).[46] Our results initially show well-balanced mobilities, with $\mu_h = (1.3 \pm 0.3) \times 10^{-5}$ cm^2 V^{-1} s^{-1} and $\mu_e = (1.4 \pm 0.3) \times 10^{-5}$ cm^2 V^{-1} s^{-1} in the PM6:IO4Cl blend under an electric field of 5×10^4 V cm^{-1}. Nevertheless, we observe a progressive degradation of device performance (i.e., lower current density and SCLC mobility) as the electron-only devices are exposed to ambient (Figure S14, Supporting Information). In fact, functional electron-only devices showing an evident SCLC regime (determined by a *J–V* slope equal to 2 in a log-log plot) could only be manufactured in inert atmosphere. Contrarily, hole-only devices did not show such behavior and could be manufactured entirely in air. Therefore, a severe SCLC mobility imbalance might arise in the OPV devices (further amplified with the elapsed time in air) that increases the *J–V* curve asymmetry (hence also that of the EQEs), as previously suggested by our drift-diffusion simulations (Figure 2d). Devices featuring thinner PALs are presumably more resilient against such mobility imbalance and its detrimental asymmetry effect on the EQE and *J–V* characteristics.

On the other hand, when examining the voltage-dependence of the experimental EQE, the wavelength-independent increase for the cathode side illumination (Figure 5b) can to some extent be explained by the current density not having saturated yet. This is supported by acquiring *J–V* curves under strong applied bias (up to −10 V, Figure S9, Supporting Information) and extracting the corresponding exciton dissociation and charge collection efficiencies (which stay <80%). However, the voltage-dependence of the anode side EQE (Figure 5a) shows a wavelength-dependent increase which cannot be solely explained by electrical effects from the dead PAL. Therefore, we suggest that the dead PAL features voltage-dependent exciton dissociation. Figure 5e,f also include the simulated EQEs for the case that the dead PAL has returned to full functionality under reverse bias (−5 V), in which case their spectral shapes reproduce well the experimental measurements (Figure 5a,b).

Regarding the underlying cause of the dead layer at the anode side of the devices, we consider the acidity of the PEDOT:PSS layer and its potentially detrimental interaction with some of the PAL components.[47] To test this hypothesis, we deposit CuSCN, a transparent inorganic semiconductor used in OPV either as donor[48] or hole transport layer, between the PEDOT:PSS and the PAL on the anode side. The CuSCN layer is expected to block any unfavorable chemical reaction between PEDOT:PSS and the PAL. However, the corresponding *J–V* curves and EQE data (Figure S15, Supporting Information) reveal that the cathode/anode asymmetry is still present. Therefore, an unfavorable PAL morphology, mostly driven by a detrimental vertical segregation or a poorly stable phase segregation upon lamination, might be explaining the observed EQE asymmetry.

2.5. *J–V* Curve Asymmetry in Further Laminated Donor:Acceptor Blends

We investigate the role played by the compatibility between donor and acceptor materials and the resulting film morphology on the asymmetric photovoltaic performance. Accordingly, we screen different donor:acceptor blends while collecting both *J–V* curves and EQE spectra upon different illumination directions. Our material selection includes PM6:3,9-bis(2-methylene-((3-(1,1-dicyanomethylene)-6,7-difluoro)-indanone))-5,5,11,11-tetrakis(4-hexylphenyl)-dithieno[2,3-*d*:2′,3′-*d*′]-*s*-indaceno[1,2-*b*:5,6-*b*′]dithiophene (IT-4F, **Figure 6**a,b), PM6:PYF-T-o (an all-polymer blend,[49] Figure 6c,d), PM6:[6,6]-phenyl-C_{61}-butyric acid methyl ester ($PC_{61}BM$, Figure 6e,f), poly[(thiophene)-*alt*-(6,7-difluoro-2-(2-hexyldecyloxy)quinoxaline)] (PTQ10):IO4Cl (Figure 6g,h), PTQ10:$PC_{61}BM$ (Figure 6i,j), and PM6:IO4Cl:$PC_{61}BM$ (Figure 6k,l). The corresponding photovoltaic figures-of-merit are detailed in Table S3 (Supporting Information). Note that in these experiments the PAL deposition (by spin coating), lamination and *J–V* curve characterization occur in inert atmosphere to disregard air-exposure degradation artifacts. EQE spectra acquisition takes place right after the *J–V* curve measurements, in air and paying close attention to minimize the device exposure to ambient air and room light.

In Figure 6, we first observe that PM6-based blends (PM6:IT-4F, PM6:PYF-T-o and PM6:$PC_{61}BM$) systematically show higher anode side J_{sc}. This is diametrically opposed to our observations in PM6:IO4Cl devices. The substitution of IO4Cl by a different NFA (IT-4F) does not show an evident filtering effect on the EQE data (Figure 6b), neither a severe cathode/anode asymmetry in terms of PCE (4.7% and 4.0% for the cathode and anode sides, respectively, see Figure 6a). The device performance is further improved when the small molecule NFA is substituted by a state-of-the-art polymer

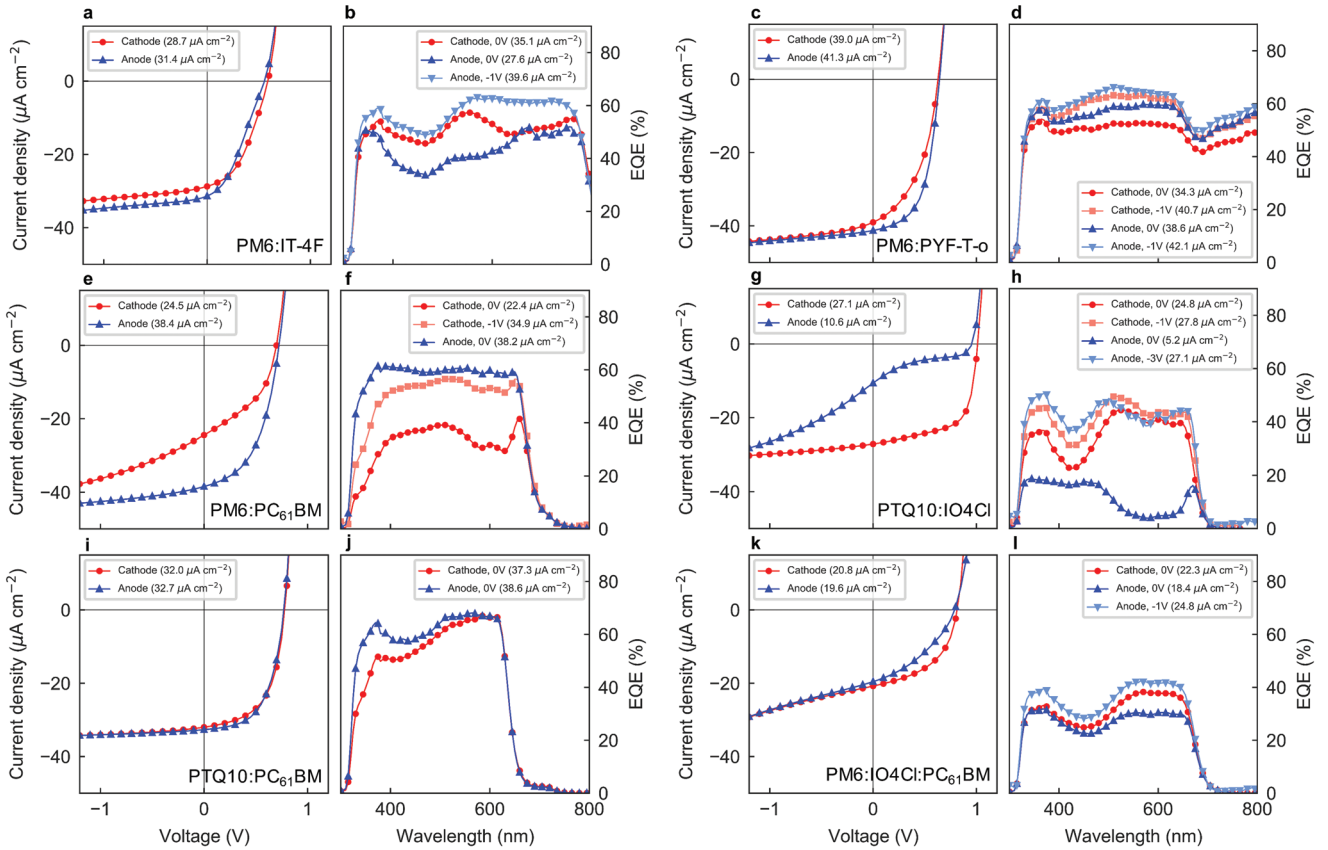

Figure 6. *J–V* curves and EQE spectra of laminated devices with different donor:acceptor combinations in the PAL: a,b) PM6:IT-4F; c,d) PM6:PYF-T-o; e,f) PM6:$PC_{61}BM$; g,h) PTQ10:IO4Cl; i,j) PTQ10:$PC_{61}BM$; and k,l) PM6:IO4Cl:$PC_{61}BM$ ternary. Values in parenthesis correspond either to the measured J_{sc} extracted from the *J–V* curves under 545 lux, or the integrated photocurrent from the EQE data (J_{EQE}).

acceptor, namely PYF-T-o.[49] PCE values get higher (7.4% and 9.8% for cathode and anode, respectively, see Figure 6c) and photocurrents are well-balanced, in excellent agreement with the observed symmetric EQE data (Figure 6d). Conversely, the PM6:$PC_{61}BM$ blend shows an acute cathode/anode asymmetry (Figure 6e) albeit with the cathode side (PCE = 4.8%) showing worse performance than the anode (PCE = 9.1%). We notice an undesirable filtering signature in the EQE data, unambiguously attributed to PM6 given its characteristic absorption features (Figure S3b, Supporting Information) at ≈600 nm (Figure 6f). We also observe that by applying a reverse bias of –1 V, the filtering effect on the cathode side is mostly removed while the anode side shows a featureless and flat EQE even at 0 V (Figure 6f). In close analogy to our previous optical modeling for PM6:IO4Cl, we have verified the effect on the device performance asymmetry in the hypothetical case in which a dead layer arises in the vicinity of the PAL/SnO_2 interface (Figure S16, Supporting Information). It is, thus, plausible that in the PM6:$PC_{61}BM$ blend either a dead PAL forms or PM6 preferentially migrates toward the PAL/SnO_2 interface. Any of these circumstances might explain the filtering effect (as per the EQE data) and the limited photovoltaic performance (as per the *J–V* curves) of PM6:$PC_{61}BM$ devices when illuminated from the cathode side. Therefore, the PAL morphology of PM6-based blends appears very sensitive to the choice of acceptor material among NFAs, polymers and fullerenes (and indirectly solvent, see Experimental Section). This behavior leads to distinctive cathode/anode *J–V* curve symmetries and might induce undesirable filtering layers evidenced in the EQE spectra of semitransparent laminated devices.

We thus consider substituting PM6 by a different donor polymer, namely the low cost and low synthetic complexity PTQ10.[50] Blending PTQ10 and IO4Cl renders a V_{oc} exceeding 1 V and a PCE of 11.6% at 545 lux when illuminated from the cathode side (Figure 6g). Surprisingly, the PCE is one order of magnitude lower (1.8%) when the device is illuminated from the anode side while the corresponding EQE shows an extremely amplified filtering effect (Figure 6h). We verify once more that by applying a reverse bias, the spectral shape of the anode side EQE resembles that of the cathode, thus confirming the existence of an anomalous thin layer of similar nature as that found previously in PM6:IO4Cl blends. This fact indicates that IO4Cl might also have its part of responsibility in the cathode/anode asymmetry in PM6:IO4Cl devices, in addition to PM6 as per the PM6:$PC_{61}BM$ data. In fact, a PTQ10:$PC_{61}BM$ blend processed following previously reported recipes[12] shows excellent indoor photovoltaic performance, including perfectly symmetric *J–V* curves (PCEs of 9.4% and 9.5% for cathode and anode, respectively; see Figure 6i) and absence of filtering layers according to EQE data (Figure 6j). Overall, these results point to the PAL morphology as the main cause of the observed cathode/anode asymmetry and the anomalous filtering layer

rather than oxygen-induced trap-assisted recombination, PAL degradation, or detrimental chemical reactions at the device interfaces. We finally explore the possibility to employ ternary blends, namely PM6:IO4Cl:$PC_{61}BM$, as a way to overcome the limitations imposed by the PM6:IO4Cl binary in terms of device performance and cathode/anode asymmetry. The *J–V* curves of the ternary blend (Figure 6k) appear better matched, with PCEs of 5.5% and 3.8% for the cathode and anode sides, respectively, yet the unsaturated reverse current (indicating current leakage in reverse bias) significantly limits the FF <50%. Interestingly, the corresponding EQE spectra (Figure 6l) appear significantly more balanced without evident filtering layers, largely resembling those of thinner binaries (Figure 4h). Therefore, our results suggest that ternary blends which combine oppositely asymmetric *J–V* binary systems (e.g., PM6:IO4Cl and PM6:$PC_{61}BM$) could provide a rational strategy toward thick, high performing, electrically symmetric and laminated NFA-based blends in the future.

3. Conclusions

Despite its promising indoor photovoltaic performance in laboratory environments, the PM6:IO4Cl blend imposes severe limitations upon air processing and lamination of thick semitransparent devices. Blade-coated PM6:IO4Cl cells in air show dissimilar performance depending on illumination side, with the cathode side generally outperforming the anode side. EQE data combined with drift-diffusion and optical modeling suggest that a filtering layer at the PAL/anode contact interface is the origin of the observed cathode/anode performance asymmetry. For the PM6:IO4Cl blend, we find that making the PAL thinner is a suitable strategy to balance cathode and anode side performances at the expense of lower PCE, even when blade coated in air. By investigating a number of spin-coated donor:acceptor binary blends in inert atmosphere, we rationalize the occurrence of cathode/anode asymmetry in thick devices to the PAL morphology and its unfavorable vertical stratification, which promote undesirable filtering layers throughout the device stack. We confirm that certain all-polymer and fullerene-based combinations, such as PM6:PYF-T-o and PTQ10:$PC_{61}BM$, show rather symmetric cathode/anode *J–V* curves and EQE spectra even on thick devices when processed in a nitrogen-filled glovebox. Eventually, we identify ternary PM6:IO4Cl:$PC_{61}BM$ blends as a promising strategy to exploit the unique properties of NFAs also in laminated organic indoor cells.

4. Experimental Section

Materials: PM6 was obtained from 1-Material (Lot# YY19116CH100). IO4Cl (batches IOC02 and IOC03) and PTQ10 (batch PQ1001) were obtained from Brilliant Matters. IT-4F was obtained from Solarmer. $PC_{61}BM$ was obtained from Solenne BV. The polymer acceptor PYF-T-o was obtained from eFlexPV (PA30 batch) and blended with PM6 from the same supplier. CuSCN, solvents and additives were purchased from Merck (Sigma–Aldrich) and used as received. The commercial SnO_2 formulation (N-31) was purchased from Avantama and used as received. PEDOT:PSS (either Clevios PH1000 for electrodes, or Clevios P VP Al 4083 for hole injection in SCLC devices) was obtained from Heraeus GmbH. Heat-stabilized PET (125 µm) Melinex ST505 (Tekra) was used as substrate.

Device Fabrication: Laminated PV cells were fabricated by laminating two stacks composed of PET/PH1000/ETL/PAL (cathode stack) to PAL/(HTL)/PH1000/PET (anode stack) using a roll laminator (GSS DH-650S Graphical Solutions Scandinavia AB) with a roll temperature of 115–130 °C (depending on the PAL materials). NFA-based blends generally required higher lamination temperature (130 °C) than fullerene or polymer-based PALs (115 °C) when working in air; however, while in the glovebox, a lamination temperature of 110–115 °C would suffice for most blends. Before proceeding with the lamination, both stacks were prepatterned with a scalpel to define the device active areas. The force between the lamination rollers was measured to ≈55 N using a force sensor (FlexiForce A201, Tekscan). Finally, the laminated devices were sandwiched between two glass slides as a mechanical support to ease their handling, and silver paint (Agar AGG302) added onto the exposed PEDOT:PSS contacts. Note that these devices were not encapsulated at any stage.

The pristine PEDOT:PSS (PH1000) with 6 vol.% ethylene glycol and 0.5 vol.% Capstone FS-30 surfactant (Dupont) was further diluted in deionized water (2:1, v/v, ink:water) before being slot-die coated (Solar X3, FOM Technologies) on PET foils. After the coating, the PEDOT:PSS layers were baked at 130 °C for 15 min. The ETL was deposited by blade coating at 5 mm s^{-1}, 80 °C and with a gap of 75 µm; or by spin coating at 2000 rpm for 30 s, and annealed (in any case) at 115 °C for 2 min in air. The blend PM6:IO4Cl (1:1.5, w/w) was dissolved in chlorobenzene (15 mg mL^{-1}) and blade coated in air at different speeds (from 15 to 2.5 mm s^{-1}), at 80 °C and setting a blade gap with respect to the PET surface of 75 µm. PM6:IO4Cl layers were not annealed before proceeding with the lamination process. PM6 and IT-4F were blended in a 1:1 (w/w) ratio in chlorobenzene:1,8-diiodooctane (99.5:0.5, v/v) at 20 mg mL^{-1}, followed by spin coating at 1000 rpm and annealed for 10 min at 100 °C in the glovebox. PM6 and PYF-T-o (1:1.2, w/w) were dissolved in *o*-xylene:1-cloronapthalene (99:1, v/v) at 15 mg mL^{-1} and spin-coated at 1000 rpm in the glovebox, followed by annealing for 5 min at 100 °C. PM6 and $PC_{61}BM$ (1:1.5, w/w) were dissolved in *o*-xylene up to a total concentration of 40 mg mL^{-1} and spin coated in the glovebox at 1000 rpm without further annealing treatments. PTQ10 and IO4Cl (1:1.5, w/w) were dissolved in chlorobenzene up to a total concentration of 40 mg mL^{-1} and spin coated in the glovebox at 1000 rpm without further annealing treatments. PTQ10 and $PC_{61}BM$ (1:1.5, w/w) were dissolved in *o*-xylene:diphenyl ether (85:15, v/v) up to a total concentration of 40 mg mL^{-1} and spin coated in the glovebox at 2000 rpm, followed by annealing for 2 min at 80 °C (as reported elsewhere).[12] PM6:IO4Cl:$PC_{61}BM$ (1:0.75:0.75, w/w/w) were dissolved in chlorobenzene (20 mg mL^{-1}) and spin coated in the glovebox at 1000 rpm without further annealing.

Single-carrier SCLC devices were manufactured on ITO-coated PET substrates to allow higher current densities and avoid detrimental series resistance. For hole-only devices, PEDOT:PSS P VP Al 4083 was first deposited as hole-injecting layer by blade coating in air at 5 mm s^{-1} and 80 °C; the pristine PEDOT:PSS was previously diluted in 2-propanol (IPA) as 1:5 (v/v, PEDOT:IPA). The film was then annealed at 130 °C for 15 min before depositing the PM6:IO4Cl by spin coating in air at 700 rpm for 60 s. Hole-only devices were laminated in air at 130 °C. For electron-only devices, a layer of SnO_2 nanoparticles (N-31, Avantama) was blade coated as electron-injecting layer following the same protocol as in photovoltaic devices. Then, the PM6:IO4Cl layer was spin coated at 700 rpm for 60 s in a nitrogen-filled glovebox. In this case, lamination took place also in the glovebox at 110–115 °C, as well as the initial *J–V* curve characterization. In both types of devices, a single piece of substrate was cut in half and laminated, thus guaranteeing perfect contact symmetry and no built-in bias.

Electrical and Optical Characterization: *J–V* curves were recorded with a Keithley 2400 SourceMeter under cool LED irradiation at a temperature of 20–25 °C. The emission spectra and irradiance of the LED source (Figure S1, Supporting Information) were measured by a high precision fiber optics spectrometer (QE-Pro, Ocean Optics) and a Hamamatsu

silicon photodiode S1133-01. Upon integration of the corresponding emission spectrum[34] acquired at the precise device location, the illuminance, the power density and the current density read 545 lux, 149.7 μW cm^{-2}, and 67 μA cm^{-2}, respectively. To avoid photodegradation, the light intensity-dependent recombination analysis was performed in a nitrogen-filled glovebox. The EQE was measured with the Spectral Response Measurement System QE-R3011 (Enli Technology Co., Ltd). Transmittance spectra were acquired with a Lambda 950 UV–vis (Perkin Elmer).

Fourier transform photocurrent spectroscopy (FTPS)-EQE was measured using a Vertex 70 from Bruker Optics, equipped with a quartz tungsten halogen lamp, quartz beam splitter, and external detector option. A low-noise current amplifier (SR570) was used to amplify the photocurrent produced on illumination of the photovoltaic devices with light modulated by the Fourier transform infrared (FTIR) spectroscope. The output voltage of the current amplifier was fed back into the external detector port of the FTIR, to be able to use the FTIR's software to collect the photocurrent spectrum.

Variable angle spectroscopic ellipsometry (VASE) data were recorded with a dual rotating compensator ellipsometer (J. A. Woollam, Co., Inc.) in the spectral range 170–1690 nm at angles of incidence in the range 45°–75° with step 10°. Modeling was performed using the software CompleteEASE (J. A. Woollam, Co., Inc.), whereby model-generated data were fitted to experimental data using non-linear regression. Films were deposited on glass substrates. The refractive index of the glass substrate was determined on a bare sample without any film deposited and then used for the film samples. For the film samples, a single-layer model (glass/film/ambient) was used with thickness and complex-valued refractive index $N = n + ik$ of the film as fit parameters. Kramers–Kronig consistent B-splines[51] were used as dispersion function for the index with restriction of positive imaginary part of the corresponding dielectric function $\varepsilon = N^2$.

Drift-Diffusion and Optical Simulations: The simulations presented in this work were performed with the Advanced Semiconductor Analysis (ASA) software, which is commercially available under https://asa.ewi.tudelft.nl/ (last accessed 11/11/2022). It includes an optical solver which was used to calculate the generation rate profile (G) on the basis of transfer matrix theory. The device stack was replicated and used in the experiments with a 125 μm PET layer on the top and bottom, which was defined to be incoherent. An 80 nm thick layer of PEDOT:PSS was added on both sides. On the cathode side, an additional 10 nm thick layer of SnO_2 was included. The PAL thickness was varied to match the experiments. After optical modeling, G was reduced by a constant factor to account for the exciton-dissociation efficiency. The resulting G could then be used for 1D drift-diffusion simulations. For the simulations with a dead PAL, the total PAL was split into electrically identical sublayers with different exciton-dissociation efficiencies. The parameters used for the simulations are listed in Tables S1 and S2 (Supporting Information). The bandgap and the Urbach energy were set to values extracted from FTPS measurements (Figure S17, Supporting Information). Also, the dark J–V characteristics were used to extract the external resistances for the simulations. Since most dark J–V curves include a non-linear shunt resistance, the following equation was used

$$J(V) = J_0\left(\exp\left[\frac{q(V - JR_S)}{n_{id}kT}\right] - 1\right) + aV^b \quad (2)$$

to fit the experimental data for the ideality factor n_{id}, the series resistance R_S, the saturation-current density J_0, the shunt-current prefactor a, and the shunt-current exponent b. While R_S can be used in the drift-diffusion simulations, the non-linear leakage current was added afterward.

Supporting Information

Supporting Information is available from the Wiley Online Library or from the author.

Acknowledgements

The authors acknowledge Dr. Lingeswaran Arunagiri (Linköping University) for his advice on preparation of all-polymer devices; Dr. Nannan Yao (Linköping University) for her help in the acquisition of the FTPS-EQE spectra; and Prof. Hans Arwin (Linköping University) for the acquisition of the ellipsometry data. X.R.-M., S.R.-G., and O.I. acknowledge the Knut and Alice Wallenberg Foundation for funding. P.H. and T.K acknowledge funding by the Helmholtz Association. F.G. acknowledges the Olle Engkvists Stiftelse and the Swedish Foundation for Strategic Research for their support.

Conflict of Interest

Mr. Thomas Österberg and Prof. Olle Inganäs are co-founders of Epishine AB, a company which focuses on laminated photovoltaic devices for indoor applications.

Data Availability Statement

The data that support the findings of this study are available from the corresponding author upon reasonable request.

Keywords

device modeling, indoor photovoltaics, organic photovoltaics, semitransparency, solution processing

Received: February 1, 2023
Revised: March 2, 2023
Published online: March 28, 2023

[1] V. Pecunia, L. G. Occhipinti, R. L. Z. Hoye, *Adv. Energy Mater.* **2021**, *11*, 2100698.
[2] I. Mathews, S. N. Kantareddy, T. Buonassisi, I. M. Peters, *Joule* **2019**, *3*, 1415.
[3] M. O. Reese, S. Glynn, M. D. Kempe, D. L. McGott, M. S. Dabney, T. M. Barnes, S. Booth, D. Feldman, N. M. Haegel, *Nat. Energy* **2018**, *3*, 1002.
[4] M. Kaltenbrunner, G. Adam, E. D. Głowacki, M. Drack, R. Schwödiauer, L. Leonat, D. H. Apaydin, H. Groiss, M. C. Scharber, M. S. White, N. S. Sariciftci, S. Bauer, *Nat. Mater.* **2015**, *14*, 1032.
[5] N. Espinosa, M. Hösel, D. Angmo, F. C. Krebs, *Energy Environ. Sci.* **2012**, *5*, 5117.
[6] G. Zhang, F. R. Lin, F. Qi, T. Heumüller, A. Distler, H.-J. Egelhaaf, N. Li, P. C. Y. Chow, C. J. Brabec, A. K.-Y. Jen, H.-L. Yip, *Chem. Rev.* **2022**, *122*, 14180.
[7] D. Lübke, P. Hartnagel, J. Angona, T. Kirchartz, *Adv. Energy Mater.* **2021**, *11*, 2101474.
[8] N. H. Reich, W. G. J. H. M. van Sark, W. C. Turkenburg, *Renewable Energy* **2011**, *36*, 642.
[9] F. Bai, J. Zhang, A. Zeng, H. Zhao, K. Duan, H. Yu, K. Cheng, G. Chai, Y. Chen, J. Liang, W. Ma, H. Yan, *Joule* **2021**, *5*, 1231.
[10] Y. Cui, Y. Wang, J. Bergqvist, H. Yao, Y. Xu, B. Gao, C. Yang, S. Zhang, O. Inganäs, F. Gao, J. Hou, *Nat. Energy* **2019**, *4*, 768.
[11] X. Li, S. Luo, H. Sun, H. H.-Y. Sung, H. Yu, T. Liu, Y. Xiao, F. Bai, M. Pan, X. Lu, I. D. Williams, X. Guo, Y. Li, H. Yan, *Energy Environ. Sci.* **2021**, *14*, 4555.
[12] X. Rodríguez-Martínez, S. Riera-Galindo, J. Cong, T. Österberg, M. Campoy-Quiles, O. Inganäs, *J. Mater. Chem. A* **2022**, *10*, 10768.

[13] J. Li, H.-L. Cao, W.-B. Jiao, Q. Wang, M. Wei, I. Cantone, J. Lü, A. Abate, *Nat. Commun.* **2020**, *11*, 310.
[14] D. Yan, X. Lu, S. Zhao, Z. Zhang, M. Lu, J. Feng, J. Zhang, K. Spencer, T. Watson, M. Li, B. Hou, F. Wang, Z. Li, *Sol. RRL* **2022**, *6*, 2200332.
[15] E. M. Hutter, R. Sangster, C. Testerink, B. Ehrler, C. M. M. Gommers, *iScience* **2022**, *25*, 103583.
[16] M. Wang, W. Wang, B. Ma, W. Shen, L. Liu, K. Cao, S. Chen, W. Huang, *Nano-Micro Lett.* **2021**, *13*, 62.
[17] Y. Peng, T. N. Huq, J. Mei, L. Portilla, R. A. Jagt, L. G. Occhipinti, J. L. MacManus-Driscoll, R. L. Z. Hoye, V. Pecunia, *Adv. Energy Mater.* **2021**, *11*, 2002761.
[18] H. S. Ryu, S. Y. Park, T. H. Lee, J. Y. Kim, H. Y. Woo, *Nanoscale* **2020**, *12*, 5792.
[19] M. Mainville, M. Leclerc, *ACS Energy Lett.* **2020**, *5*, 1186.
[20] A. Tang, B. Xiao, Y. Wang, F. Gao, K. Tajima, H. Bin, Z. Zhang, Y. Li, Z. Wei, E. Zhou, *Adv. Funct. Mater.* **2018**, *28*, 1704507.
[21] Y. Xu, Y. Cui, H. Yao, T. Zhang, J. Zhang, L. Ma, J. Wang, Z. Wei, J. Hou, *Adv. Mater.* **2021**, *33*, 2101090.
[22] Q. Wu, Y. Yu, X. Xia, Y. Gao, T. Wang, R. Sun, J. Guo, S. Wang, G. Xie, X. Lu, E. Zhou, J. Min, *Joule* **2022**, *6*, 2138.
[23] Z. Wang, A. Tang, H. Wang, Q. Guo, Q. Guo, X. Sun, Z. Xiao, L. Ding, E. Zhou, *Chem. Eng. J.* **2023**, *451*, 139080.
[24] C. J. Brabec, A. Distler, X. Du, H. Egelhaaf, J. Hauch, T. Heumueller, N. Li, *Adv. Energy Mater.* **2020**, *10*, 2001864.
[25] J. Guo, Y. Wu, R. Sun, W. Wang, J. Guo, Q. Wu, X. Tang, C. Sun, Z. Luo, K. Chang, Z. Zhang, J. Yuan, T. Li, W. Tang, E. Zhou, Z. Xiao, L. Ding, Y. Zou, X. Zhan, C. Yang, Z. Li, C. J. Brabec, Y. Li, J. Min, *J. Mater. Chem. A* **2019**, *7*, 25088.
[26] D. Zhang, B. Fan, L. Ying, N. Li, C. J. Brabec, F. Huang, Y. Cao, *SusMat* **2021**, *1*, 4.
[27] A. Ghaffari, Z. Saki, N. Taghavinia, M. M. Byranvand, M. Saliba, *Mater. Horiz.* **2022**, *9*, 2473.
[28] X. Rodríguez-Martínez, S. Riera-Galindo, L. E. Aguirre, M. Campoy-Quiles, H. Arwin, O. Inganäs, *Adv. Funct. Mater.* **2022**, *33*, 2213220.
[29] J. Bergqvist, T. Österberg, A. Melianas, L. E. Aguirre, Z. Tang, W. Cai, Z. Ma, M. Kemerink, D. Gedefaw, M. R. Andersson, O. Inganäs, *npj Flexible Electron.* **2018**, *2*, 4.
[30] N. Li, B. E. Lassiter, R. R. Lunt, G. Wei, S. R. Forrest, *Appl. Phys. Lett.* **2009**, *94*, 023307.
[31] K. Vandewal, K. Tvingstedt, A. Gadisa, O. Inganäs, J. V. Manca, *Nat. Mater.* **2009**, *8*, 904.
[32] G. Burwell, O. J. Sandberg, W. Li, P. Meredith, M. Carnie, A. Armin, *Sol. RRL* **2022**, *6*, 2200315.
[33] G. F. A. Dibb, M.-A. Muth, T. Kirchartz, S. Engmann, H. Hoppe, G. Gobsch, M. Thelakkat, N. Blouin, S. Tierney, M. Carrasco-Orozco, J. R. Durrant, J. Nelson, *Sci. Rep.* **2013**, *3*, 3335.
[34] Y. Cui, L. Hong, T. Zhang, H. Meng, H. Yan, F. Gao, J. Hou, *Joule* **2021**, *5*, 1016.
[35] S. Khan, M. Gui, X. Liu, N. C. Giebink, A. Kahn, B. P. Rand, *Adv. Energy Mater.* **2022**, *12*, 2200551.
[36] T. Upreti, S. Wilken, H. Zhang, M. Kemerink, *J. Phys. Chem. Lett.* **2021**, *12*, 9874.
[37] C. M. Stafford, K. E. Roskov, T. H. Epps, M. J. Fasolka, *Rev. Sci. Instrum.* **2006**, *77*, 023908.
[38] A. Sánchez-Díaz, X. Rodríguez-Martínez, L. Córcoles-Guija, G. Mora-Martín, M. Campoy-Quiles, *Adv. Electron. Mater.* **2018**, *4*, 1700477.
[39] C. J. Traverse, R. Pandey, M. C. Barr, R. R. Lunt, *Nat. Energy* **2017**, *2*, 849.
[40] S. R. Cowan, A. Roy, A. J. Heeger, *Phys. Rev. B* **2010**, *82*, 245207.
[41] T. Kirchartz, J. Nelson, *Phys. Rev. B* **2012**, *86*, 165201.
[42] T. Kirchartz, F. Deledalle, P. S. Tuladhar, J. R. Durrant, J. Nelson, *J. Phys. Chem. Lett.* **2013**, *4*, 2371.
[43] L. J. A. Koster, V. D. Mihailetchi, H. Xie, P. W. M. Blom, *Appl. Phys. Lett.* **2005**, *87*, 203502.
[44] A. K. K. Kyaw, D. H. Wang, V. Gupta, W. L. Leong, L. Ke, G. C. Bazan, A. J. Heeger, *ACS Nano* **2013**, *7*, 4569.
[45] C. van Berkel, M. J. Powell, A. R. Franklin, I. D. French, *J. Appl. Phys.* **1993**, *73*, 5264.
[46] J. C. Blakesley, F. A. Castro, W. Kylberg, G. F. A. Dibb, C. Arantes, R. Valaski, M. Cremona, J. S. Kim, J.-S. Kim, *Org. Electron.* **2014**, *15*, 1263.
[47] J. Cameron, P. J. Skabara, *Mater. Horiz.* **2020**, *7*, 1759.
[48] F. Eisner, B. Tam, V. Belova, W. Ow, J. Yan, M. Azzouzi, A. Kafizas, M. Campoy-Quiles, A. Hankin, J. Nelson, *Cell Rep. Phys. Sci.* **2021**, *2*, 100676.
[49] H. Yu, M. Pan, R. Sun, I. Agunawela, J. Zhang, Y. Li, Z. Qi, H. Han, X. Zou, W. Zhou, S. Chen, J. Y. L. Lai, S. Luo, Z. Luo, D. Zhao, X. Lu, H. Ade, F. Huang, J. Min, H. Yan, *Angew. Chem., Int. Ed.* **2021**, *60*, 10137.
[50] C. Sun, F. Pan, H. Bin, J. Zhang, L. Xue, B. Qiu, Z. Wei, Z.-G. Zhang, Y. Li, *Nat. Commun.* **2018**, *9*, 743.
[51] B. Johs, J. S. Hale, *Phys. Status Solidi* **2008**, *205*, 715.